

THE EXTRAGALACTIC LENS VLBI IMAGING SURVEY (ELVIS).

I. A SEARCH FOR THE CENTRAL IMAGE IN THE GRAVITATIONAL LENS PMN J1838–3427

EDWARD R. BOYCE^{1,2}, JOSHUA N. WINN¹, JACQUELINE N. HEWITT¹, AND STEVEN T. MYERS²

Draft version December 26, 2018

ABSTRACT

The Extragalactic Lens VLBI Imaging Survey (ELVIS) searches for central images of lensed radio quasars, in order to measure the central density profiles of distant galaxies. Here we present sensitive multi-epoch Very Long Baseline Array (VLBA) observations of PMN J1838–3427 at 8 GHz, with a 1σ noise level of $38\ \mu\text{Jy beam}^{-1}$. Based on the absence of a central image of the background source at this level, we explore the possibilities for the central matter distribution in the lens galaxy. A power-law density profile, $\rho \propto r^{-\gamma}$, must have $\gamma > 1.93$. Thus the density profile is close to an isothermal profile ($\gamma = 2$) or steeper. The upper limit on any constant-density core in an otherwise isothermal profile is $\lesssim 5$ parsecs. We also derive the constraints on models in which the density profile is isothermal on kiloparsec scales, but is allowed to have a different power law in the central ~ 100 parsecs. If the lens galaxy harbors a supermassive black hole, the galaxy profile is allowed to be shallower, but for the expected black hole mass the galaxy profile must still be close to isothermal or steeper.

Subject headings: gravitational lensing — galaxies: elliptical and lenticular, cd

1. INTRODUCTION

The central regions of galaxies ($r < 1$ kpc) are a topic of great interest, but one for which it is difficult to compare the results of observations and theoretical simulations. The observational difficulty is especially severe for galaxies at cosmological distances. The Extragalactic Lens VLBI Imaging Survey (ELVIS) is motivated mainly by the desire to measure (or place interesting constraints on) the central matter distribution in galaxies at significant redshift, by searching for central images of gravitational lenses. As this is the first ELVIS publication, we elaborate on the theoretical and observational situation.

On the theoretical side, cosmological dark matter simulations produce dark matter halos with a universal density profile that goes as $\rho \propto r^{-3}$ at large radii and $\rho \propto r^{-\gamma}, \gamma = 1 - 1.5$ at small radii (Navarro et al. 1997; Moore et al. 1999). The transition occurs at a scale radius r_s , typically $10 - 30$ kpc for halos of galactic mass. The main difficulty with interpreting the results for galaxy interiors is that on scales ~ 10 kpc and smaller, the baryonic component is expected to modify the dark matter halo significantly. Adiabatic contraction (Blumenthal et al. 1986) and similar models (Sellwood & McGaugh 2005) model the contraction of dark matter under the gravitation of a baryonic disk or bulge. The total matter profile steepens and becomes close to isothermal ($\rho \propto r^{-2}$) on scales of a few kpc (Kazantzidis et al. 2006). Similar results are found from hydrodynamic simulations that use cooling, gas dynamics, star formation and gravitation to model the dark matter and baryons within individual halos. The baryonic matter dissipates energy and collects at the halo center, becoming the dominant component inside radii $1.5 - 5$ kpc (Gnedin et al.

2004; Macciò et al. 2006). The dark matter contracts inwards under the gravitational influence of the baryons, again giving a total matter profile that is close to isothermal. At present the smallest scales probed by the hydrodynamic simulations are $0.3 - 1$ kpc.

On the observational side, the density distributions of massive galaxies can be directly probed through dynamical studies, at least in the nearby universe. Gerhard et al. (2001) have modelled the dynamics of a sample of large early-type galaxies, using photometry and kinematic line profiles. The dark matter fraction is only $10 - 40\%$ within the effective radius R_e , while the rotation curves are flat on scales larger than $0.2R_e$, indicating an isothermal density profile on these scales. Typically $R_e = 4 - 10$ kpc (Kronawitter et al. 2000), so these results agree with the simulations described above. The density profile of an early type galaxy is isothermal at radii of a few kpc, and baryons represent most of the mass inside this radius.

Projected surface brightness profiles of nearby galaxies ($z = 0.002 - 0.005$) have been observed with the Hubble Space Telescope (Lauer, T. R. et al. 1995). The angular resolution is $0''.1$, which corresponds to a physical size of ~ 10 pc for the typical galaxy in this sample. The surface brightness profiles are well fit by a broken power law, with steep outer exponents, shallower inner exponents, and break radii between 10 and 1000 pc. Based on their inner profiles $I(R) \propto R^{-\beta}$ the galaxies can be classified into two populations: steep cusps with $\beta \sim 1$ and flatter cores with $\beta = 0 - 0.3$. A surface density power law $\Sigma(R) \propto R^{-\beta}$ corresponds to a density power law $\rho(r) \propto r^{-\gamma}$, where $\gamma = \beta + 1$. Thus the luminous matter in a cuspy galaxy has an isothermal distribution ($\Sigma(R) \propto R^{-1}$) to within ~ 10 pc of the galaxy’s center, while the luminous matter in a core galaxy breaks to a shallower profile at some radius $\lesssim 1$ kpc. This is a good approximation to the total mass profile, as the stars seem to represent most of the mass at these radii.

Gravitational lenses provide information on the mass profiles of more distant (and therefore younger) galaxies. For a lens galaxy at $z = 0.3 - 1.0$, the relative positions

Electronic address: eboyce@mit.edu, jwinn@space.mit.edu, jhewitt@space.mit.edu, smyers@nrao.edu

¹ Department of Physics and Kavli Institute for Astrophysics and Space Research, Massachusetts Institute of Technology, 77 Massachusetts Avenue, Cambridge MA 02139

² National Radio Astronomy Observatory, PO Box O, Socorro NM 87801

and fluxes of the bright lensed images of a background source constrain the matter profile interior to a few kpc from the lens galaxy center. Detailed studies of ~ 20 gravitational lenses find that the early type lens galaxies have density profiles which are very close to isothermal on these scales (Rusin et al. 2003; Koopmans et al. 2006). Distant early-type galaxies have similar profiles to those nearby: they are isothermal at galactic radii of a few kpc.

But what about the central few hundred parsecs? Here, too, gravitational lenses can help, through the properties of the “central image.” In theory, a non-singular galactic profile produces an odd number of images (Dyer & Roeder 1980; Burke 1981). One image forms near the center of the lens galaxy, where it is expected to be highly demagnified by the large surface density at that position (Narasimha et al. 1986). Due to the demagnification, the faint central image is rarely observed, leaving two or four bright images. In cases where the density profile is singular, with a central cusp that is stronger than isothermal ($\rho \sim r^{-\gamma}$ with $\gamma \geq 2$), no central image is produced even in theory.

While they are hard to observe, central images probe the inner 10–100 pc of very distant galaxies. Winn et al. (2003, 2004) have confirmed the existence of a central image produced by an isolated lens galaxy in the lens PMN J1632-0033, using radio observations. We discuss this object and its matter profile further in Section 5. Inada, N. et al. (2005) found a central image generated by the combined profile of a cluster and a massive galaxy, using the Sloan Digital Sky Survey and the Hubble Space Telescope (HST). The mass modelling here is dependent on both the galaxy and the cluster profile.

Most galaxies host a super-massive black hole (SMBH) whose mass correlates closely with the properties of the central stellar bulge (Kormendy & Richstone 1995; Magorrian, J. et al. 1998), particularly the velocity dispersion (the $M - \sigma$ relation; Ferrarese & Merritt (2000); Gebhardt, K. et al. (2000); Tremaine, S. et al. (2002)). A SMBH in the lens galaxy affects the central image: it can destroy the central image, or split the central image into two images, one of which is directly attributable to the black hole (Mao et al. 2001; Bowman et al. 2004). In the latter case, the properties of the central-image pair could allow for the measurement of the black hole mass in an ordinary galaxy at significant redshift (Rusin et al. 2005).

Based on the surface-brightness profiles of nearby early-type galaxies measured with HST, Keeton (2003) predicted the distribution of core image magnifications. He found a broad distribution, from $10^{-4.5}$ to 10^{-1} , with a most probable magnification of approximately $10^{-2.5}$. Adding a SMBH had little effect on central-image detectability: the magnification of the central image was strongly affected only when the magnification of the galaxy alone was already very low. Rusin & Ma (2001) placed limits on central mass distributions using radio observations of six lenses from the Cosmic Lens All-Sky Survey (CLASS; Browne, I. W. A. et al. (2003); Myers, S. T. et al. (2003)). Their basic result was that if the density profiles in the lens galaxies are taken to be power laws in radius, then they must be nearly isothermal or steeper. The constraints were somewhat weaker when a SMBH was included.

This paper is organized as follows. Section 2 describes

the design of our survey. Section 3 presents new observations of our first target, PMN J1838–3427. Section 4 presents models for the density profile in the lens galaxy of this system, and the final section summarizes the results.

2. ELVIS

The Extragalactic Lens VLBI Imaging Survey (ELVIS) will involve sensitive, high-angular-resolution radio observations of many of the known cases of gravitational lensing of a radio-loud quasar. The traditional reasons to conduct such observations are to confirm cases of gravitational lensing, and to observe correspondences between lensed radio jets in order to refine models of the lens galaxy. ELVIS is the first survey (to our knowledge) motivated by the search for central images. As such, our highest-priority targets are those that are most favorable for central-image hunting: radio-loud, asymmetric two-image lenses.

The asymmetric two-image lenses (those with a large magnification ratio between the two bright quasar images) are best because for those systems, the mean magnification of the central image is generally the largest, for a given lens galaxy (Mao et al. 2001; Bowman et al. 2004). In a highly asymmetric system, the angular separation between the lens galaxy and the unlensed source is nearly as large as possible, while still being close enough to produce multiple images. This results in a central image that is as distant as possible from the lens galaxy center. More symmetric systems (especially those that produce four bright images) have central images located closer to the galaxy center, where the surface density is larger and the degree of demagnification is consequently greater.

Observing at radio wavelengths is desirable to avoid extinction by dust within the interstellar medium of the lens galaxy. Attenuation by plasma effects is also possible, but can be minimized by observing at a high enough radio frequency (typically ≥ 5 GHz). Moreover, an optical image could easily be lost in the starlight of the lens galaxy, while even a demagnified radio image will be brighter than a typical radio-quiet lens galaxy. The angular separation between the central image and the other images, or the lens galaxy center, is likely to be 100 mas or less, so at the widely used radio frequencies of 1-10 GHz, very-long-baseline interferometry (VLBI) is needed.

The search for central images is a task that is well-matched to recent advances in VLBI technologies. New high-bandwidth recorders and digital back-ends have increased typical data rates by a factor of 4 in recent years, with even greater improvements expected in the next few years. The effect is a considerable sensitivity boost for those experiments that can take advantage of the increased bandwidth. The European VLBI Network now routinely records at 1 Gb s^{-1} . The U.S. National Radio Astronomy Observatory does not yet generally deploy recorders with bandwidths this wide, but it recently began devoting approximately 300 hours per year to simultaneous observing with the 10-station Very Long Baseline Array (VLBA) and several other large antennas such as the phased Very Large Array (VLA), Arecibo, the Green Bank Telescope, and the Effelsberg telescope. The thermal noise level with this “High Sensitivity Ar-

TABLE 1
DETAILS OF THE VLBA OBSERVATIONS.

Date	Image A point source (mJy)	flux density total (mJy)	Image B flux density (mJy)	R.A. _A -R.A. _B	dec. _A -dec. _B	Blank field rms (μ Jy beam $^{-1}$)
2000 Oct 07	206.8	219.2	9.3	0. ⁰ 09747	0. ⁰ 99130	86
2000 Oct 30	204.3	213.4	16.2	0. ⁰ 09747	0. ⁰ 99125	88
2000 Dec 17	222.4	232.3	12.8	0. ⁰ 09746	0. ⁰ 99122	95
2000 Dec 18	202.7	214.4	12.3	0. ⁰ 09747	0. ⁰ 99121	98
2000 Dec 22	209.7	209.7	13.4	0. ⁰ 09745	0. ⁰ 99118	93
2001 Mar 24	207.5	219.5	18.3	0. ⁰ 09744	0. ⁰ 99111	79

NOTE. — Details of the individual observing epochs. The beam size varied slightly between epochs, with average values of 3.5×1.3 mas, and the position angle was always within 1° of zero. All epochs excluded the Brewster antenna due to low elevations. The December epochs lacked the North Liberty VLBA antenna, December 17 and December 18 substituted a single Very Large Array (VLA) antenna for the Pie Town VLBA antenna.

ray" (HSA) is often 10-20 times lower than a traditional VLBA observation of similar duration. Gravitational lens central image searches are perfect projects for sensitive observations with heterogeneous arrays. The search for a faint central image in an otherwise blank region is a problem limited mainly by the thermal noise level, rather than the need for complete coverage of the Fourier plane. The typical radio lens field has two or four bright, compact sources (the bright images of the lensed quasar), and no extended structure. The bright images provide in-beam phase calibration sources. The simplicity of the source structure (multiple, isolated point sources) makes it easier to calibrate and image the data from the heterogeneous array.

For all these reasons, the first ELVIS targets are radio-loud quasars lensed by a single galaxy to produce two bright images with a flux ratio exceeding 5:1. Two lenses that fit this description, PMN J1632-0033 (Winn, J. N. et al. 2002) and CLASS B1030+074 (Xanthopoulos, E. et al. 1998), have already been the subjects of sensitive VLBI observations by other groups. In the former case, good evidence for a central image was found (Winn et al. 2004). We are in the process of obtaining data from long-duration VLBA observations, or shorter-duration HSA observations, of the other known radio lenses meeting these criteria, many of which are taken from CLASS.

Here we present our first target, PMN J1838-3427. This gravitational lens was discovered by Winn, J. N. et al. (2000), as part of a survey for radio-loud gravitational lenses in the southern sky. It has a two bright images separated by $1.^{\circ}0$ and with a flux ratio of 14:1. The redshift of the source quasar is at $z_S = 2.78$. A spectroscopic redshift for the lens galaxy has not been measured, despite several attempts. It is a difficult measurement mainly because the optical light of the lens galaxy is blended with that of the fainter lens image, and also because the system resides in a crowded field at low galactic latitude. Winn, J. N. et al. (2000) estimated $z_L = 0.36 \pm 0.08$, the range of redshifts for which the lens galaxy photometry is consistent with the fundamental plane relation. The source was monitored at 9 GHz with the Australia Telescope Compact Array (Winn, J. N. et al. 2004), as discussed in Section 3.1.

3. OBSERVATIONS OF J1838-3427

We observed PMN J1838-3427 (hereafter, J1838) with the ten antennas of the NRAO Very Long Baseline Ar-

ray (VLBA), on 6 different epochs between 2000 October and 2001 March. At each epoch, the duration of the observation was 5 hours. We observed right circular polarization with a central frequency of 8.415 GHz. We used 2 bit sampling at 16 Msamples s $^{-1}$ for each of 8 channels, giving a total data rate of 256 Mb s $^{-1}$. Data from antennas that were observing at an elevation of less than 10 degrees were excluded (this included all of the data from the Brewster antenna). In addition, the North Liberty antenna was not in use for two epochs, and was excluded from a third epoch for which its data were very noisy and degraded the image. Thus, 3 epochs used 9 antennas and 3 epochs used 8 antennas. In each observation, the time on J1838 was 4.5 hours and the estimated thermal noise limit (based on the collecting area and receiver characteristics) was $\sim 70 \mu$ Jy beam $^{-1}$.

For each epoch the data were amplitude calibrated in AIPS, following standard procedures. Because image A of the gravitational lens is fairly bright, with a flux density of ~ 200 mJy, we did not need to perform phase referencing. The initial phase solution was derived from a fringe fit to a point-source model centered at the location of image A, using a solution interval of 2 minutes. We then reduced the data with nine self-calibration cycles, each cycle consisting of imaging, phase-only self-calibration with a 0.5-1.5 minute solution interval, imaging, and phase and amplitude self-calibration with a 15 minute solution interval. For each new cycle, smaller CLEAN components were included.

The brightest image A appeared as a point source of flux ~ 210 mJy, with ~ 10 mJy of extended emission to the west, while image B appeared as a point source, varying between 9 and 18 mJy. Maps from the first epoch are shown in Figure 2, while details of each observing run are presented in Table 1. The single epoch 5 GHz VLBA map of Winn, J. N. et al. (2000) shows two bright point sources at the same positions, with diffuse emission to the west of image A. The fraction of the total image A flux density in this extended component is $\sim 10\%$ at 5 GHz and $\sim 5\%$ at 8.4 GHz, so the extended emission has a steeper spectral index than the point source.

The flux densities of the two bright images varied between the epochs, and the ratio of these flux densities also varied. The image A to image B flux density ratio in our maps varies from 12 to 24, with an average of 15. This ratio averaged 14.6 in VLA observations and 10.6 in

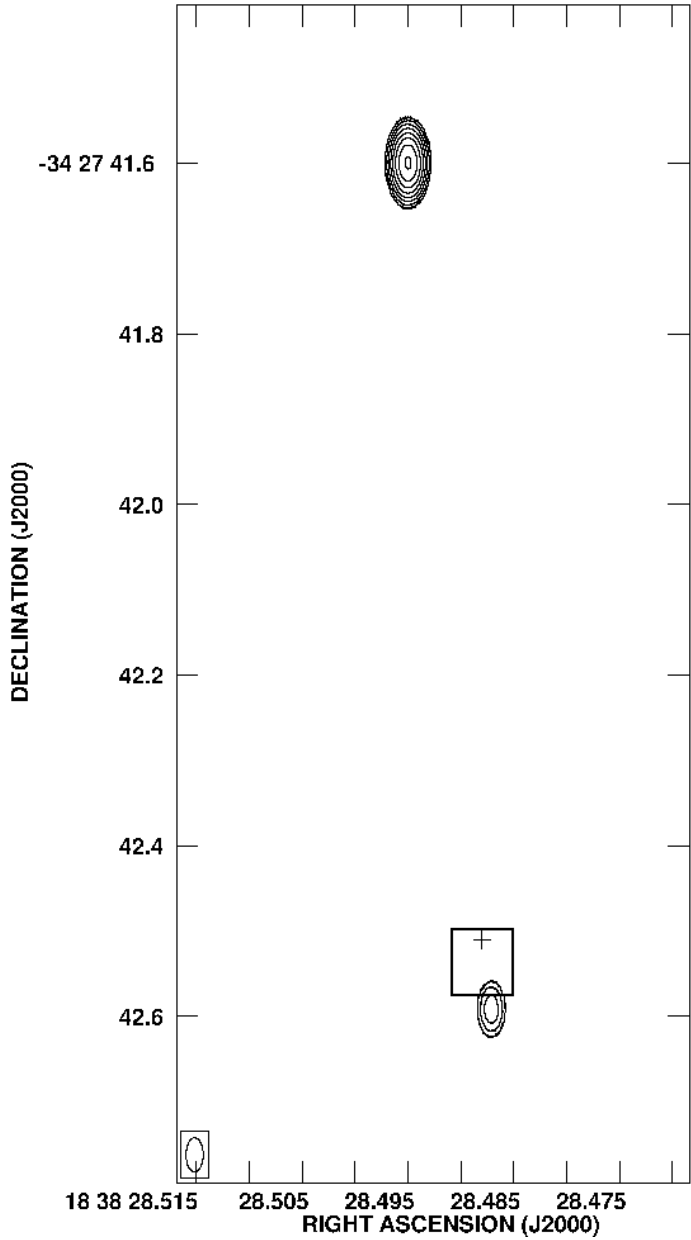


FIG. 1.— Radio map of the two images of gravitational lens PMN J1838-3427, made with the VLBA at 8 GHz. Data are from the first epoch. The restoring beam (40×20 mas) was chosen to be much larger than the naturally weighted beam in order to show both images on a single map. Contours begin at $1.5 \text{ mJy beam}^{-1}$ and increase by factors of 2. The J2000 radio positions were not determined from our observations; they were assumed from earlier VLA imaging. The cross marks the location of the lens galaxy detected using HST/WFPC2; its position is based on the offset from the bright quasar images in the WFPC2 images. The box shows the central image search region.

the the previous 5 GHz VLBA observations (Winn, J. N. et al. 2000). The lens images appear to undergo large variations in intensity. The two most obvious possible explanations are intrinsic source variation, and interstellar scintillation (see Section 3.1).

No additional sources of radiation were seen in any epoch. We examined a large region between the location of the lens galaxy and the bright image B, where a cen-

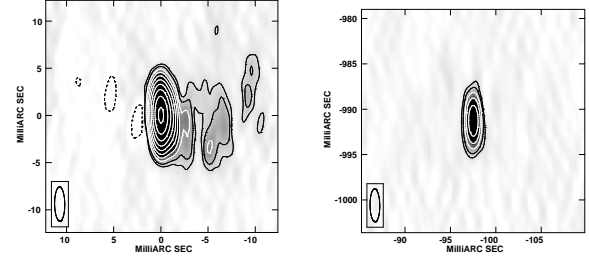


FIG. 2.— (left) Radio map of image A. (right) Radio map of image B. Both maps were made from the first epoch of VLBA imaging at 8 GHz. Coordinate offsets are from the phase center at (J2000) $18^{\text{h}}34^{\text{m}}28^{\text{s}}495$, $-34^{\circ}27'41''.60$. Contours begin at $300 \mu\text{Jy beam}^{-1}$ and increase by factors of 2 (the blank field rms near image B was $86 \mu\text{Jy beam}^{-1}$). The synthesized beam of 3.6×1.1 mas is shown at the lower left. Note the extended emission to the west of the main point source in image A.

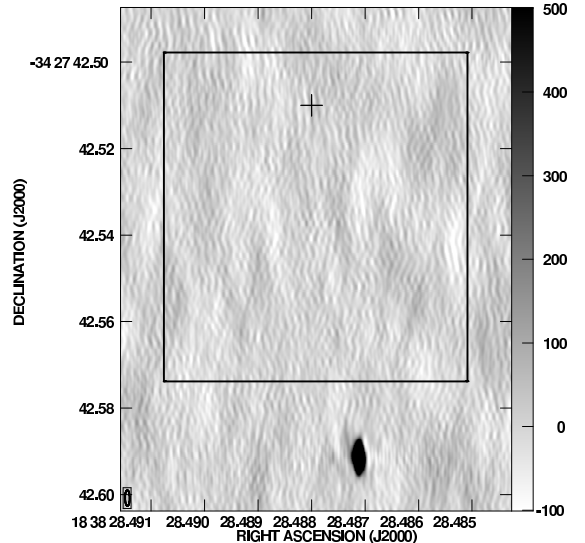


FIG. 3.— Radio map of the central image search region, from the combined VLBA 8 GHz map of all six epochs. The wedge at right shows the grey scale in $\mu\text{Jy beam}^{-1}$. The J2000 radio positions were not determined from phase referencing; they were assumed from earlier VLA imaging. The cross marks the location of the lens galaxy detected using HST/WFPC2. Its position is based on the offset from the bright quasar images in the WFPC2 images. Image B is obvious near the bottom of the map. The central image would form at the light travel time maximum located between the lens galaxy and the bright image B, so we searched for the central image in the boxed area.

tral image would be expected.³ We extended this region slightly to the other side of the lens galaxy to allow for the uncertainty in the optical position. From epoch to epoch the noise varied from $79 \mu\text{Jy beam}^{-1}$ to $98 \mu\text{Jy beam}^{-1}$ (Table 1), which is within 20-30% of the expected thermal noise limit. The small but significant excess over the thermal noise limit is expected, given the southerly declination of the target. When the six maps were co-added,

³ Gravitational lens images form at extrema of the time delay surface, which is a combination of the geometric delay and the lens galaxy potential determined by its density profile. The central image forms near the lens galaxy potential maximum. The geometric delay shifts the overall maximum towards the saddle point image B, on the opposite side of the lens galaxy from the source. The central image will thus form between the lens galaxy and image B, the fainter of the two bright images.

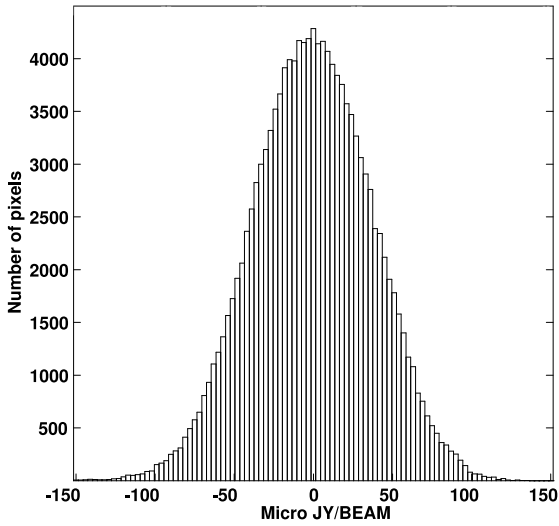


FIG. 4.— Histogram of surface brightness values for all pixels within the central-image search region. The pixel size is 0.2 mas, which is smaller than the typical beam size of 3.5×1.3 mas. The distribution of surface brightness is approximately Gaussian, with a mean of $-0.4 \mu\text{Jy beam}^{-1}$ and a standard deviation of $38 \mu\text{Jy beam}^{-1}$.

the central-image search region remained blank (see Figure 3) and the noise decreased by $\sim \sqrt{6}$. The distribution of surface brightness in the pixels of the final map is roughly Gaussian, with a mean of $-0.4 \mu\text{Jy beam}^{-1}$ and a standard deviation of $38 \mu\text{Jy beam}^{-1}$ (see Figure 4).

To quote an upper limit, we considered directly the surface brightness distribution and took the 99th percentile to be the 99% limit on the central image flux density. This gave an upper limit on the central image flux density of $S_C < 83 \mu\text{Jy}$, and a lower limit on the magnification ratio of the brightest image to the central image of $S_A/S_C > 2500$, both with 99% confidence. For comparison, the 5 GHz VLBA maps of Winn, J. N. et al. (2000) reached an rms of $190 \mu\text{Jy beam}^{-1}$, and measured a flux density of $S_A = 145 \text{ mJy}$ for the brightest image. Assuming a Gaussian distribution for the blank field errors, the old 99% limits were $S_C < 470 \mu\text{Jy}$ and $S_A/S_C > 310$.

3.1. Scintillation

We found the flux densities S_A and S_B of the two bright quasar images to vary from epoch to epoch. The ratio S_A/S_B also varied significantly, demonstrating that the variations are not due only to inconsistencies in the flux density scale. Image B showed a higher fractional variation than image A (Table 1). This is similar to what was observed by Winn, J. N. et al. (2004), who monitored this object for 4 months with the Australia Telescope Compact Array (ATCA) at 9 GHz. Over the course of the campaign, the fractional variation in the flux density of image A was 4%, and that of image B was 8%.

The lens is located at a low galactic latitude ($b_{\text{II}} = -12^\circ.5$), and may undergo scintillation due to the Milky Way's interstellar medium. The root-mean-squared amplitude due to scintillation is inversely proportional to the angular size of the source (Walker 1998, 2001), while the

angular size of each lens image is proportional to $S^{1/2}$, since gravitational lensing conserves surface brightness. Thus the rms amplitude of scintillation variations is proportional to $S^{-1/2}$, and the fainter image B would be more affected by interstellar scintillation than image A. In contrast, intrinsic variability should produce the same fractional variation in each component (though the variations would appear with time lags due to the geometric and Shapiro delays). The greater fractional variation of image B that was observed with ATCA, and in our own observations, supports the scintillation hypothesis.

The central image, if it exists, has a much smaller flux density and angular size than either of the bright images. Taking $S_A/S_C > 2500$, scintillation would cause fractional variations in S_C of order unity. No central radio source was seen in any individual observation. Scintillation, if present, did not magnify the central image above the detection limit for any single epoch ($\sim 200 \mu\text{Jy}$). In what follows, we use the blank field of the combined map to define our upper limit on the central image flux density, but we note that scintillation could be a major source of systematic error in this determination.

4. MASS MODELS

4.1. Cuspy Matter Profiles

With this new and more stringent upper limit on the flux density of the central image, we can restrict the possibilities for the central density profile of the J1838 lens galaxy. A simple and realistic model for the mass distribution of a massive galaxy is a broken power law (see Section 1). We adopt the broken power law density profile of Muñoz et al. (2001), in which the surface density and the deflection angle are given by analytic expressions. This profile varies as $\rho \propto r^{-n}$ at large radii, and as $\rho \propto r^{-\gamma}$ at small radii, with a break at radius r_b :

$$\rho(r) = \frac{\rho_0}{r^\gamma} \frac{1}{(1 + r^2/r_b^2)^{(n-\gamma)/2}}. \quad (1)$$

Since galactic profiles are approximately isothermal on scales of a few kpc (see Section 1) and we have few constraints, we apply the method used by Winn et al. (2003) in the analysis of PMN J1632–0033 and fix the outer power law to be isothermal ($n = 2$). We then explore the constraints on the break radius r_b and inner power law index γ . In the limit of a pure isothermal sphere, the central image vanishes; thus, as r_b goes to zero or as γ goes to 2, the central image flux density approaches zero. We use a spherical galaxy model, and account for non-sphericity in the profile with an external shear at an arbitrary position angle. The 10 free parameters of our model are the positions of the lens galaxy and the source, (x_G, y_G, x_S, y_S) , the source flux (S_S), the mass parameter ($b = (2\pi r_b \rho_0)/(\Sigma_{cr})$)⁴ the shear and its position angle (s, θ_s), the break radius (r_b) and the inner power law index (γ).

The data provide 9 observables: the two sky coordinates for each of the lens galaxy, bright image A and bright image B; the flux densities for image A and image

⁴ The quantity $\Sigma_{cr} = (c^2/4\pi G)(D_S/(D_L D_{LS}))$ is the critical surface density for lensing. The quantities D_L , D_S and D_{LS} are the angular diameter distances from the observer to the lens, from the observer to the source and from the lens to the source, respectively.

TABLE 2
LENS MODEL CONSTRAINTS.

Observable	Value
R.A. _A	0 ⁰ 000 \pm 0 ⁰ 003
decl. _A	0 ⁰ 000 \pm 0 ⁰ 003
R.A. _B	-0 ⁰ 9912 \pm 0 ⁰ 003
decl. _B	-0 ⁰ 0975 \pm 0 ⁰ 003
R.A. _G	-0 ⁰ 911 \pm 0 ⁰ 006
decl. _G	-0 ⁰ 085 \pm 0 ⁰ 006
S_A	208.3 \pm 41.8 mJy
S_B	13.7 \pm 2.7 mJy
S_C	0.000 \pm 0.038 mJy

NOTE. — Constraints on the lens models, with 1σ errors. All positions are offsets from image A. Galaxy positions are from the WFPC2 photometry in Winn, J. N. et al. (2000), other constraints are from the VLBA data.

B (S_A, S_B); and an upper limit on the flux density of the central image C (S_C). The galaxy coordinates and their uncertainties were taken from the Hubble Space Telescope Wide Field Planetary Camera 2 (WFPC2) photometry by Winn, J. N. et al. (2000). The radio coordinates and flux densities for images A and B were measured in each of the six VLBA maps and the mean values of these observables were taken as model constraints. We considered only the bright peak of image A, and ignored the diffuse emission to the west, as we consider only the point source magnifications. Since both the positions and fluxes of the bright images may be perturbed by substructure in the lens galaxy, we adopted errors of 3 mas in the positions and 20% in the flux densities (cf. Mao & Schneider (1998); Keeton & Kochanek (1998); Kochanek et al. (2004)). The constraint on S_C was taken from the rms noise in a large region between the lens galaxy position and image B in the combined VLBA image. The distribution of surface brightness in the pixels of this blank region was approximately Gaussian, with a mean of $-0.4 \mu\text{Jy beam}^{-1}$ and a standard deviation of $38 \mu\text{Jy beam}^{-1}$ (see Figure 4). We took this to be a null detection of the central image with a 1σ error of $38 \mu\text{Jy beam}$, and set $S_C = 0 \pm 38 \mu\text{Jy}$ for the modelling. These constraints are summarized in Table 2. All of the observables were assumed to obey Gaussian statistics, and 1σ error bars are quoted.

We model the lens with the *gravlens* package by Keeton (2001). For the conversion from angular units to physical units, we assume $z_L = 0.36$ and a ΛCDM cosmology with $H_0 = 70 \text{ km s}^{-1} \text{ Mpc}^{-1}$, $\Omega_m = 0.3$, $\Omega_\Lambda = 0.7$. With 10 free parameters and 9 measurements, one would expect a one-dimensional locus of allowed points in parameter space. In fact, because the observable S_C is an upper limit, the data define a one-dimensional boundary between an allowed region and a disallowed region in parameter space. In Figure 5, we plot the projection of this plane in the r_b, γ parameter space that characterizes the inner density profile. Values of the other parameters are given in Table 3 for the isothermal case ($r_b = 2$ or $\gamma = 0$), and these values change by $\lesssim 10\%$ over the region of r_b, γ parameter space we investigated.

For a sufficiently small break radius r_b or sufficiently steep inner index γ , the model fits the data perfectly. As r_b increases or γ decreases, the fits become progressively

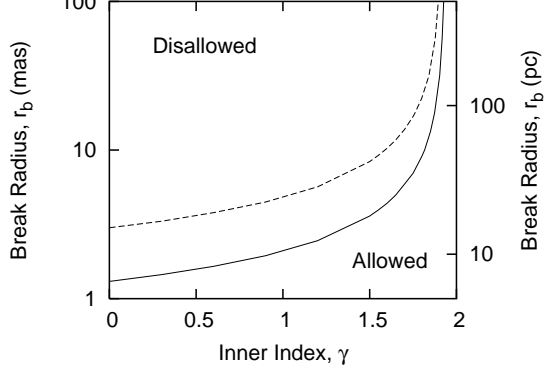


FIG. 5.— Models for the lens galaxy of PMN J1838-3427, using the new data presented in this paper (solid line) and the previous data from Winn, J. N. et al. (2000) (dashed line). The matter profile is isothermal ($\rho \propto r^{-2}$) at large radius, and goes as $\rho \propto r^{-\gamma}$ at small radius, with the break at radius r_b . The inner power law index and break radius are allowed to vary. The lines mark the $\chi^2 = 5.99$ boundary between the allowed region (below and to the right) and the disallowed region (above and to the left). The break radius in parsecs is calculated for $z_L = 0.36$.

TABLE 3
LENS MODEL PARAMETERS FOR THE ISOTHERMAL CASE.

Parameter	Value
$b = \theta_E$	0 ⁰ 528
x_G	-0 ⁰ 0850
y_G	-0 ⁰ 9109
x_S	-0 ⁰ 0187
y_S	-0 ⁰ 4747
S_S	80.3 mJy
s	0.0649
θ_s	-18 ⁰ 1

NOTE. — The best fit values of the lens model parameters for the isothermal case (when $r_b = 0$ or $\gamma = 2$).

worse and χ^2 becomes large. Most of the disagreement is due to an unacceptably large S_C . Near the boundary of the allowed region the best fits give slight variations in the calculated values for the other observables, but these are generally less than the 1σ errors. The 95% confidence region ($\chi^2 < 5.99$ for two free parameters, cf. Bevington & Robinson (2003)) lies below and to the right of the solid line. The matter distribution is nearly isothermal: a flat core with $\gamma = 0$ must be very small ($r_b \lesssim 1.5 \text{ mas} \approx 5 \text{ pc}$), and a large core with $r_b = 100 \text{ mas} \approx 500 \text{ pc}$ has a steep inner profile ($\gamma \gtrsim 1.92$).

For comparison, Figure 5 includes the region of parameter space allowed by the less stringent observational constraints of Winn, J. N. et al. (2000). The new data reduce the maximum size of a flat core by a factor of ~ 2.5 , and increase the minimum inner index of a large core by ~ 0.05 .

4.2. Cuspy Matter Profiles with Black Holes

Most elliptical galaxies host super-massive black holes at their centers (Kormendy & Richstone 1995; Magorrian, J. et al. 1998): this additional point mass steepens the overall central profile and may demagnify the central image (Mao et al. 2001). A realistic galaxy model should include a central black hole. As seen in the previous

section, even an interesting smooth profile is underconstrained. To avoid adding extra degrees of freedom to the model, we add a black hole with a fixed mass given by the $M - \sigma$ relation (Ferrarese & Merritt 2000; Gebhardt, K. et al. 2000; Tremaine, S. et al. 2002), and determine the resulting effect.

For an early-type lens galaxy, most of the mass will be in the bulge component and so the total mass responsible for the lensing is a good estimate of the overall velocity dispersion. To estimate σ , we determine the best-fitting value of the Einstein radius using a model consisting of an isothermal sphere and external shear, and then use the relation $\theta_E = 4\pi(D_{\text{LS}}/D_S)(\sigma^2/c^2)$. For the broken power law model, the mass normalization parameter $b = (2\pi r_b \rho_0)/(\Sigma_{cr})$ is equivalent to θ_E and this parameter varies by $< 10\%$ over the allowed region in the broken power law models, so the isothermal θ_E is a good estimate of the true velocity dispersion even if the true density profile is not exactly isothermal.

Given this estimate for σ , we calculate the black hole mass M_{bh} using the relation from Tremaine, S. et al. (2002),

$$M_{\text{bh}} = 1.35 \times 10^8 M_{\odot} \left(\frac{\sigma}{200 \text{ km s}^{-1}} \right)^{4.02}. \quad (2)$$

For J1838, $\theta_E = 0''.523$, $\sigma = 154 \text{ km s}^{-1}$ and $M_{\text{bh}} = 4.7 \times 10^7 M_{\odot}$. The scatter in the $M - \sigma$ relation is 0.3 dex (Tremaine, S. et al. 2002), so a plausible range for the black hole mass is $2.5 \times 10^7 - 1.0 \times 10^8 M_{\odot}$.

We rerun the calculations from Section 4.1, but this time include a point mass fixed at the center of the lens galaxy. We consider a black hole with mass $5 \times 10^7 M_{\odot}$, in the center of the expected range, and a black hole with the mass $10^8 M_{\odot}$, at the top of the expected range. The black hole either eliminates the central image completely, leaving only the two bright images, or creates two faint central images, the core and SMBH images, for a total of four images. The allowed regions, again defined by $\chi^2 < 5.99$, are shown in Figure 6. Below and to the right of the allowed lines there are no central images, or both the core and SMBH images are sufficiently faint that they would not have been detected in our observations. The long-dashed line is for the $5 \times 10^7 M_{\odot}$ black hole, the short-dashed line is for the $10^8 M_{\odot}$ black hole.

The separation of the core and SMBH images is 2 – 5 mas, so these might appear as a single unresolved component if aligned with the long axis of the beam. The core image flux density is greater than the SMBH image flux density by a factor of 15 – 100, so the core image flux density makes a much larger contribution to χ^2 . For models near the boundary of the allowed region, combining both central images into a single unresolved component would raise χ^2 by < 0.6 , and the allowed region would be only slightly more constrained.

The SMBH allows the galaxy profile to be shallower, to some extent. For fairly flat cores ($\gamma \lesssim 1.5$) the maximum break radius increases by about 50% for the $5 \times 10^7 M_{\odot}$ black hole, and by a factor of 2.5 – 3 for the $10^8 M_{\odot}$ black hole. For larger, cuspy cores, the minimum inner slope is reduced by ~ 0.1 for the $5 \times 10^7 M_{\odot}$ black hole and by ~ 0.2 for the $10^8 M_{\odot}$ black hole. While the central smooth profile remains close to isothermal, it is allowed to be somewhat flatter. The cusp in the profile from the black hole makes the central mass profile sufficiently

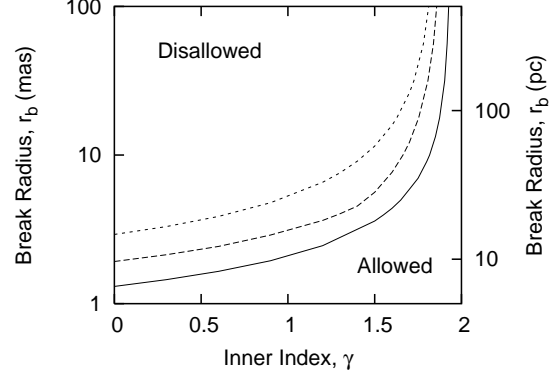


FIG. 6.— Models for the lens galaxy of PMN J1838-3427, using the new data presented in this paper and including the effects of a super-massive black hole. The matter profile is isothermal ($\rho \propto r^{-2}$) at large radius, and goes as $\rho \propto r^{-\gamma}$ at small radius, with the break at radius r_b . To the smooth matter profile we add no black hole (solid line), a $5 \times 10^7 M_{\odot}$ black hole (long-dashed line), or a $10^8 M_{\odot}$ black hole (short-dashed line). These black hole masses are the central and largest values expected, given the velocity dispersion of the galaxy. The inner power law index and break radius are allowed to vary. The lines mark the $\chi^2 = 5.99$ boundary between the allowed region (below and to the right) and the disallowed region (above and to the left). The break radius in parsecs is calculated for $z_L = 0.36$. When no black hole is present, a central image always forms within the parameter ranges plotted. In the allowed region, the central image is below our detection limit. When a black hole is present, the central image is either eliminated or split into a core image and SMBH image. In the allowed region, either there are no central images or both central images have flux densities below our detection limit.

steep even if the smooth component is shallower.

4.3. Comparison with Other Central-Image Modelling

Winn et al. (2003) modelled PMN J1632-0033, the lens with a confirmed central image, using the same cuspy profile as this work. Given that the central image is detected with a definite flux, the allowed region in the break radius and inner index space becomes a narrow band (see Winn et al. (2003), Figure 6). A flat core has a fixed small size, and a larger core is forced to a particular value of the inner index. The allowed band for J1632 is similar to the boundary of the allowed region for J1838: a central image of definite flux density selects a narrow band giving that value for S_C , while an upper limit on the central flux density selects a half plane bounded by the band for the maximum allowed S_C .

Other central image modelling has focused on single power law models. Winn et al. (2003) also considered a single power law model $\rho \propto r^{-\gamma}$ for the density profile of J1632, finding $\gamma = 1.91 \pm 0.02$. This modelling did not include a central black hole. Rusin & Ma (2001) modelled the gravitational lenses CLASS B0739+366 and B1030+074 using a single power law model for the projected surface density $\Sigma(R) \propto R^{-\beta}$, both with and without a central black hole with a mass inferred from the $M - \sigma$ relation. Their only constraint was the limit on the bright image to central image magnification ratio, the observable which dominates χ^2 in our modelling. Their limits on the smooth profile were $\beta > 0.85$ for B0739+366 and $\beta > 0.91$ for B1030+074, while the respective limits were $\beta > 0.84$ and $\beta > 0.83$ when a black hole was included.

Modelling J1838 as a single power law in the density $\rho \propto r^{-\gamma}$, we find $\gamma > 1.93$ for the smooth profile, $\gamma > 1.86$ when we include a central black hole of $5 \times 10^7 M_\odot$ and $\gamma > 1.82$ when we include a central black hole of $10^8 M_\odot$ (the central and largest values expected from the velocity dispersion). Again, we note that a surface density index β is equivalent to a density index $\gamma = \beta + 1$, so these 4 lenses are similar. The profile is slightly shallower than isothermal for J1632–0033, and the profiles are slightly shallower than or steeper than isothermal for J1838–3427, B0739+366 and B1030+074.

5. CONCLUSIONS

We have presented new VLBA data for the gravitational lens PMN J1838–3427, and set a stringent upper limit of $83 \mu\text{Jy}$ (99% confidence) on the observed flux density of the central image. The corresponding limit on the brightest image to central image magnification ratio is $S_A/S_C > 2500$. This improves on the limits observed by Winn, J. N. et al. (2000) by a factor of 8. The bright images have different flux densities and different flux density ratios in our six epochs, confirming the fluctuations seen by Winn et al. (2003). The larger fractional variation in image B relative to image A is suggestive of scintillation. The possibility that the central image also undergoes scintillation is a source of systematic uncertainty in the interpretation of the upper limit on S_C .

Lens galaxies at $z \lesssim 0.5$ have isothermal profiles on scales of a few kiloparsecs (Rusin et al. 2003; Koopmans et al. 2006), and we find that the lens galaxy in J1838 maintains this steep profile to within a few tens of parsecs of its center. The lenses J1632–0033, B0739+366 and B1030+074 also have central density profiles close to isothermal (Winn et al. 2003; Rusin & Ma 2001). These four lens galaxies resemble the nearby cusp galaxies in the photometric observations of Lauer, T. R. et al.

(1995). Galaxy simulations which track both dark matter and baryons predict isothermal profiles at galactic radii $\gtrsim 1$ kpc (see Section 1), and central image constraints from these galaxies show these profiles continuing to smaller radii. A black hole with a mass estimated from the $M - \sigma$ relation weakens the constraints somewhat, allowing the central profile to be a little more shallow.

As we add more galaxies to the ELVIS sample, we will have a larger sample of gravitational lenses with either central images or very good upper limits on the central image flux density. Central images are very sensitive to the central matter distributions that are just shallower than the isothermal profiles of many local galaxies and of distant galaxies at larger radii. With more well-constrained central matter profiles, we can determine if most early type galaxies at $z \sim 0.5$ have cuspy central profiles, or if some have shallow cores. As well as the central image from the galaxy core, we may detect central image pairs and directly measure black hole masses in distant galaxies.

We thank David Rusin and Chuck Keeton for their participation in ELVIS, and for their role in developing the lens modeling methodology used in this paper. We also thank them, Shep Doeleman, and Scott Gaudi for helpful consultations. We thank the referee for useful suggestions that considerably improved this paper. Support for this work was provided by the National Science Foundation through grant AST 00-71181. E.B. acknowledges the support of an NRAO pre-doctoral fellowship. The National Radio Astronomy Observatory is a facility of the National Science Foundation operated under cooperative agreement by Associated Universities, Inc.

Facilities: NRAO (VLBA).

REFERENCES

Bevington, P. R. & Robinson, D. K. 2003, Data Reduction and Error Analysis for the Physical Sciences, 3rd edn. (New York, NY: McGraw-Hill)

Blumenthal, G. R., Faber, S. M., Flores, R., & Primack, J. R. 1986, ApJ, 301, 27

Bowman, J. D., Hewitt, J. N., & Kiger, J. R. 2004, ApJ, 617, 81

Browne, I. W. A. et al. 2003, MNRAS, 341, 13

Burke, W. L. 1981, ApJ, 244, L1

Dyer, C. C. & Roeder, R. C. 1980, ApJ, 238, L67

Ferrarese, L. & Merritt, D. 2000, ApJ, 539, L9

Gebhardt, K. et al. 2000, ApJ, 539, L13

Gerhard, O., Kronawitter, A., Saglia, R. P., & Bender, R. 2001, AJ, 121, 1936

Gnedin, O. Y., Kravtsov, A. V., Klypin, A. A., & Nagai, D. 2004, ApJ, 616, 16

Inada, N. et al. 2005, PASJ, 57, L7

Kazantzidis, S., Zentner, A. R., & Kravtsov, A. V. 2006, ApJ, accepted, astro-ph/0510583

Keeton, C. R. 2001, astro-ph/0102340

—. 2003, ApJ, 582, 17

Keeton, C. R. & Kochanek, C. S. 1998, in Proceedings of Golden Lens Conference at JBO, <http://www.jb.man.ac.uk/research/gravlens/workshop1/prcdngs.html>

Kochanek, C. S., Schneider, P., & Wambsganss, J. 2004, in Proceedings of the 33rd Saas-Fee Advanced Course, ed. G. Meylan, P. Jetzer, & P. North (Springer-Verlag)

Koopmans, L. V. E., Treu, T., Bolton, A. S., Burles, S., & Moustakas, L. A. 2006, ApJ, submitted, /astro-ph/0601628

Kormendy, J. & Richstone, D. 1995, ARA&A, 33, 581

Kronawitter, A., Saglia, R. P., Gerhard, O., & Bender, R. 2000, A&AS, 144, 53

Lauer, T. R. et al. 1995, AJ, 110, 2622

Macciò, A. V., Moore, B., Stadel, J., & Diemand, J. 2006, MNRAS, accepted, astro-ph/0506125

Magorrian, J. et al. 1998, AJ, 115, 2285

Mao, S. & Schneider, P. 1998, MNRAS, 295, 587

Mao, S., Witt, H. J., & Koopmans, L. V. E. 2001, MNRAS, 323, 301

Moore, B., Quinn, T., Governato, F., Stadel, J., & Lake, G. 1999, MNRAS, 310, 1147

Muñoz, J. A., Kochanek, C. S., & Keeton, C. R. 2001, ApJ, 558, 657

Myers, S. T. et al. 2003, MNRAS, 341, 1

Narasingha, D., Subramanian, K., & Chitre, S. M. 1986, Nature, 321, 45

Navarro, J. F., Frenk, C. S., & White, S. D. M. 1997, ApJ, 490, 493

Rusin, D., Keeton, C. R., & Winn, J. N. 2005, ApJ, 627, L93

Rusin, D., Kochanek, C. S., & Keeton, C. R. 2003, ApJ, 595, 29

Rusin, D. & Ma, C.-P. 2001, ApJ, 549, L33

Sellwood, J. A. & McGaugh, S. S. 2005, ApJ, 634, 70

Tremaine, S. et al. 2002, ApJ, 574, 740

Walker, M. A. 1998, MNRAS, 294, 307

—. 2001, MNRAS, 321, 176

Winn, J. N., Rusin, D., & Kochanek, C. S. 2003, ApJ, 587, 80

—. 2004, Nature, 427, 613

Winn, J. N. et al. 2000, AJ, 120, 2868

—. 2002, AJ, 123, 10

—. 2004, AJ, 128, 2696

Xanthopoulos, E. et al. 1998, MNRAS, 300, 649